OET | Opto-Electronic Technology

CN 51-1811/O4 ISSN (Print) 2097-6003 ISSN (Online) 2097-8006

A 4096-element 3D-integrated Si-SiN optical phased array for high-power coherent LiDAR

Han Wang, Weimin Xie, Xin Yan, Jiaqi Li, Youxi Lu, Ping Jiang, Feng Li*, Kai Jin*, Xu Yang, Jiali Jiang, Keran Deng, Weishuai Chen, Jing Luo, Li Jin, Junbo Feng and Kai Wei*

Citation: Wang H, Xie WM, Yan X, et al. A 4096-element 3D-integrated Si-SiN optical phased array for high-power coherent LiDAR. *Opto-Electron Technol* **2**, 260009 (2026).

https://doi.org/10.29026/oet.2026.260009

Received: 6 March 2026; Accepted: 24 March 2026; Published online: 30 March 2026

Opto-Electronic Technology

Article

March 2026, Vol. 2, No. 1

Open Access

A 4096-element 3D-integrated Si-SiN optical phased array for high-power coherent LiDAR

Han Wang[1,2], Weimin Xie[1,2], Xin Yan[1,2], Jiaqi Li[1,2], Youxi Lu[4], Ping Jiang[4], Feng Li[3]*, Kai Jin[1,2]*, Xu Yang[3], Jiali Jiang[3], Keran Deng[5], Weishuai Chen[4], Jing Luo[4], Li Jin[4], Junbo Feng[4] and Kai Wei[1,2]*

Abstract: Integrated optical phased arrays (OPAs) are pivotal for next-generation solid-state light detection and ranging (LiDAR), offering high-speed, inertia-free beam steering in a compact form factor. However, achieving high angular resolution alongside multi-watt emission power remains a formidable challenge. In this work, we present a 3D-integrated silicon-silicon nitride (Si-SiN) hybrid OPA comprising 4096 (4 × 1024) elements, packaged with a CMOS driver chip via flip-chip bonding. The proposed heterogeneous Si-SiN architecture leverages PN carrier-depletion phase shifting with sub-nanosecond response capability, currently demonstrating a 2 μs CMOS-driven beam switching time and ultra-low-power (1.5 μW/π), while delivering an angular resolution of 0.038° × 0.017° (FWHM) and a total main-lobe CW emission power of 1.5 W at a 20 W high-power injection. This approach effectively circumvents silicon's nonlinear limitations while maintaining high-density integration. System-level validations include indoor coherent detection and a four-channel phase-locked synthetic aperture scheme that successfully compresses the beam divergence to 300 μrad. This architecture provides a scalable roadmap for the development of high-performance, long-range solid-state LiDAR systems.

Keywords: optical phased array (OPA); silicon photonics; solid-state LiDAR

DOI: 10.29026/oet.2026.260009 | CSTR: 32419.14.oet.2026.260009

Citation: Wang H, Xie WM, Yan X et al. A 4096-element 3D-integrated Si-SiN optical phased array for high-power coherent LiDAR. *Opto-Electron Technol* **2**, 260009 (2026).

1 Introduction

Driven by the rapid advancement of autonomous driving, robotic navigation, and three-dimensional (3D) mapping technologies, light detection and ranging (LiDAR) has emerged as a cornerstone of modern perception systems, owing to its high-precision active sensing capabilities[1–3]. Compared to radio detection and ranging (RADAR), LiDAR offers distinct advantages in terms of higher angular resolution and superior ranging accuracy[4–6], effectively bridging the gap between visible light and microwave detection modalities.

Based on ranging principles, LiDAR systems can be categorized into time-of-flight (ToF), frequency-modulated continuous wave (FMCW), and random-modulated continuous wave (RMCW) architectures based on physical entropy or pseudo-random binary sequences (PRBS)[7–9]. Regarding beam steering mechanisms, LiDAR systems are generally categorized into three architectures: mechanical scanning, semi-solid-state scanning and solid-state scanning. In comparison to mechanical and semi-solid-state configurations, solid-state LiDAR which utilizes flash[10], metasurface[11], optical phased arrays (OPA)[4], and focal plane arrays (FPA)[12], exhibits clear advantages in terms of vibration resistance, operational lifespan, and compactness[13].

The concept of the OPA originates from microwave phased array (MPA), enabling inertia-free and solid-state beam steering by controlling the phase of individual emitter elements. Since optical wavelengths are several orders of magnitude shorter than those in the microwave spectrum,

Received: 6 March 2026

Accepted: 24 March 2026

Published online: 30 March 2026

[1]State Key Laboratory of Extreme Photonics and Instrumentation, Zhejiang Key Laboratory of Autonomous Optoelectronic Perception, College of Optical Science and Engineering, Zhejiang University, Hangzhou 310027, China; [2]ZJU-Hangzhou Global Scientific and Technological Innovation Center, Zhejiang University, Hangzhou 311215, China; [3]National Laboratory on Adaptive Optics, Chengdu 610209, China; [4]United Microelectronics Center Co., Ltd (CUMEC), Chongqing 401332, China; [5]Chongqing Normal University, College of Physics and Optoelectronic Engineering, Chongqing 401331, China.

*Correspondence: F Li, E-mail: lifeng@ioe.ac.cn; K Jin, E-mail: hijk1990@zju.edu.cn; K Wei, E-mail: kwei@zju.edu.cn

OPAs facilitate significantly smaller emitter dimensions and spacings, allowing for more compact, high-density array integration. Driven by advancements in silicon photonics, on-chip integrated OPAs based on material platforms such as silicon-on-insulator (SOI), silicon nitride (SiN), and thin-film lithium niobate (LNOI) have been realized, enabling the integration of an entire OPA onto a footprint smaller than 2 cm × 2 cm while substantially reducing power consumption and cost. Furthermore, OPAs can also be implemented using alternative material platforms, including liquid crystals[14], phase-change materials, and organic compounds[10,15].

Currently, one-dimensional (1D) OPAs can achieve 2D scanning by leveraging the dispersive effects of gratings in conjunction with wavelength tuning; however, this approach is often constrained by the limited tuning range and high-speed requirements of broadband tunable lasers[16]. While two-dimensional (2D) OPA arrays offer agile and flexible beam steering, they are hindered by high device integration density and the complexity of control and drive electronics[17].

Beyond LiDAR, OPAs have demonstrated significant potential in various fields, including optical communications[18−23], spatial beamforming[24−27], optical tweezing[28], biological sensing[29,30], 3D printing[31], and imaging[32,33]. Nevertheless, these demonstrations remain largely confined to laboratory settings. The transition to practical application scenarios depends heavily on the comprehensive performance of OPAs regarding scanning speed, resolution, output power, and field of view (FOV). Significant progress has been made in these areas in recent years. High-speed solid-state scanning has been achieved through phase control mechanisms such as thermo-optic[34,35], plasma dispersion[36−38], and electro-optic (EO) effects[39−41]. Individual OPAs have already achieved angular resolutions better than 1 mrad[4], while the coherent combining and phase locking of multiple OPA apertures can further compress the divergence angle[42]. Furthermore, optimized grating antenna designs have expanded the FOV[40,43,44] and suppressed side lobes[45], effectively mitigating far-field aliasing issues. Additionally, SiN waveguides ensure minimal propagation loss and high power tolerance, with reported continuous-wave (CW) power handling up to 5 W[37] and pulse peak powers of 24 W (10 ns, 100 kHz)[46]. However, due to the inherent trade-offs between various design metrics—specifically the conflict between high-speed steering, high-power distribution, and large-scale integration—realizing an OPA that simultaneously achieves these goals remains significantly challenging. Overcoming these hurdles is a critical milestone for the transition of OPAs from laboratory demonstrations to mature commercial systems.

In this work, we demonstrate a 3D-integrated silicon-silicon nitride (Si-SiN) hybrid OPA LiDAR operating in the C-band with 4096 (4 × 1024) elements. The silicon photonics chip (Si-PIC), integrated with CMOS driver ICs via flip-chip bonding, is maintained within 2 cm × 2 cm. The device features a large emission aperture of 8 mm × 5 mm, achieving a beam divergence (FWHM) of 0.038° (600 μrad) in the phase direction (θ) and 0.017° (300 μrad) in the wavelength direction (ϕ). The phase control units utilize the carrier dispersion effect in silicon, with a power consumption of approximately 1 mW per element and a measured beam steering response time in the 2 μs regime. To evaluate the performance of the proposed OPA LiDAR, we first present its architectural design and fabrication process, followed by comprehensive device-level characterization. We subsequently demonstrate the high-power handling capability of the device, achieving stable radiation with a total main-lobe power of 1.5 W under 20 W injection. Furthermore, we demonstrate the coherent detection capability by imaging targets at a distance of 10 m in an indoor environment. Finally, the potential for performance enhancement through a closed-loop phase-locked synthetic aperture scheme—utilizing multi-aperture spatial tiling and coherent combining—is showcased, successfully compressing the beam divergence to 300 μrad. These demonstrations underscore the significant potential of OPAs for long-range, high-performance solid-state LiDAR applications.

2 Design and fabrication of the optical phased array LiDAR

The primary architecture of the 4096-element OPA chip integrates edge couplers, an optimized optical power distribution network (PDN), PN carrier-depletion phase shifters, and large-aperture grating antennas (Fig. 1). The edge couplers utilize mode-field converters to facilitate efficient transition from external optical fibers to on-chip sub-micron waveguides. To ensure uniform phase and amplitude distribution across the massive array, the PDN partitions the input light equally into each phase control unit using a multi-stage tree-like splitter configuration. By applying independent phase shifts across the array, agile beam steering in the far-field phase direction (θ) is achieved. The light is then radiated into free space via the grating antennas, where the dispersive properties of the grating enable dual-axis scanning in the wavelength direction (ϕ). This scanning mechanism is mathematically described by the standard phased array and grating equations:

$$\sin\theta = \frac{\Delta\Phi \cdot \lambda}{2\pi \cdot d}, \tag{1}$$

$$\sin\phi = n_{\mathrm{eff}}(\lambda) - m\frac{\lambda}{\Lambda}, \tag{2}$$

where $\Delta\Phi$ is the phase increment between adjacent elements, d is the element pitch, $n_{\mathrm{eff}}(\lambda)$ is the wavelength-dependent effective refractive index, Λ is the grating period, and m is the diffraction order.

To achieve milliradian-level angular resolution and a wide FOV, the system requires a large emission aperture coupled with a sub-wavelength element pitch. This necessitates high-density integration. We addressed these requirements using

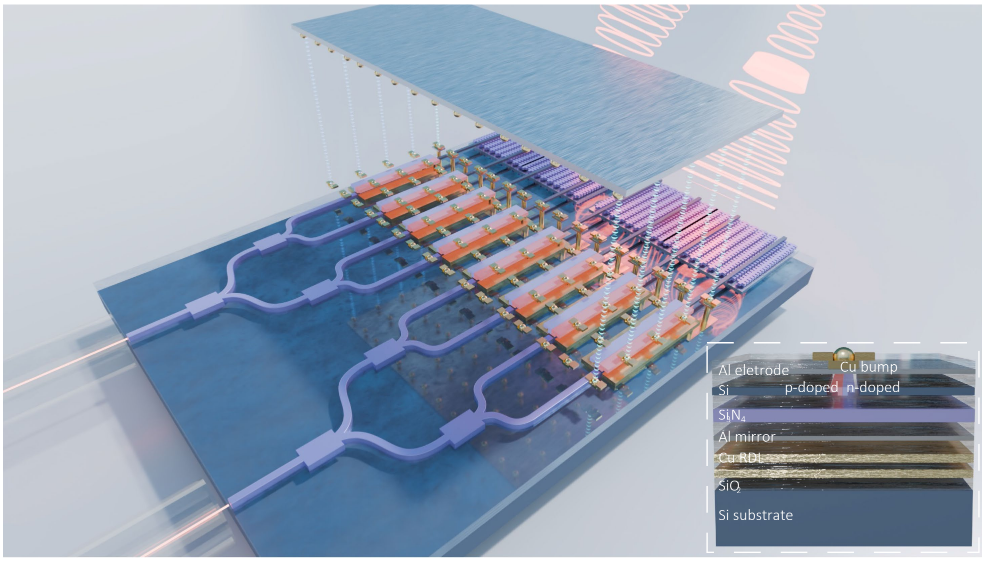

Fig. 1 | Schematic of the large-scale Si-SiN heterogeneously integrated OPA. A C-band laser beam from the source and amplifier is coupled into the chip via edge couplers and uniformly distributed to each phase-shifting unit through a multi-stage power distribution network. A flip-chip bonded CMOS IC achieves phase control by applying electrical signals to the PN carrier-depletion phase shifters, which is then radiated into free space through the grating antennas. Adjacent apertures can function as a receiver (R_X) array, where the optical path is reciprocal to the emission; the collected light is eventually coupled back into the fibers for characterization by detectors.

a Si-SiN heterogeneous integration platform, complemented by backside multi-layer metallization and wafer bonding (Fig. 2(a)). While the SOI platform offers high index contrast for compact routing, it suffers from nonlinear losses such as two-photon absorption (TPA) and subsequent free-carrier absorption (FCA) under high-power injection. In contrast, the SiN layer, characterized by its wide bandgap and low thermo-optic coefficient, provides a high power-handling threshold and ultra-low propagation loss. Adiabatic tapers are utilized to facilitate low-loss mode transition between the Si and SiN layers, allowing for a strategic design where phase modulation occurs in the active Si layer, while high-power distribution and radiation are handled by the robust SiN/Si hybrid structures.

Since even Silicon Nitride (SiN) waveguides exhibit a limited power-handling threshold at the facet coupling regions under excessive power densities—where waveguide losses can progressively increase or even lead to catastrophic thermal damage[46], and the resulting heat generation severely degrades chip performance—the input light is coupled via four independent fibers to maximize on-chip output power and enable compact transmit/receive (T_x/R_x) integration. Each channel corresponds to 1024 elements and can be flexibly assigned to any T_x/R_x configuration.

To avoid evanescent crosstalk between waveguides and enhance the output beam performance, the array element pitch is designed at 2 μm, resulting in a FOV of 45° in the phase direction. Wavelength-based beam steering leverages the dispersive effect of the grating antennas, providing a steering efficiency of 0.138°/nm through wavelength tuning. The radiation efficiency and beam profile are further optimized through structural designs. Backside wafer bonding was employed to incorporate metal mirrors beneath the grating array, effectively suppressing downward leakage and enhancing upward radiation efficiency. Furthermore, we developed a Si-SiN hybrid multi-layer grating antenna. By introducing periodic SiN perturbations beneath the silicon waveguide, the effective emission aperture is significantly enlarged, and the antenna insertion loss is minimized to approximately 2 dB. Additionally, the increased silica cladding thickness (~5 μm) provided by wafer bonding reduces the substrate leakage of the edge couplers, lowering their insertion loss to ~1 dB. The total chip insertion loss is approximately 10 dB.

The scaling of array elements to 4096 leads to a substantial increase in the density of electrical interconnects. To solve this, we implemented a backside redistribution layer (RDL) process. The dual-layer copper (Cu) RDL is specifically designed to manage the electrical routing complexity and pad-matching requirements of the 4096-element array. The high-density fan-out from 9363 bumps requires a complex interconnect network to align the PIC signal pitch with the specific pad configuration of the CMOS driver ASIC. The use of dual-layer RDLs provides the necessary routing capacity to handle thousands of channels while effectively preventing electrical traces from being positioned near the grating antennas, thereby avoiding spatial obstruction and parasitic interference with the emitted optical beam. Furthermore, this process framework significantly enhances electrical routing flexibility and scalability, providing a highly adaptable foundation for future on-chip designs

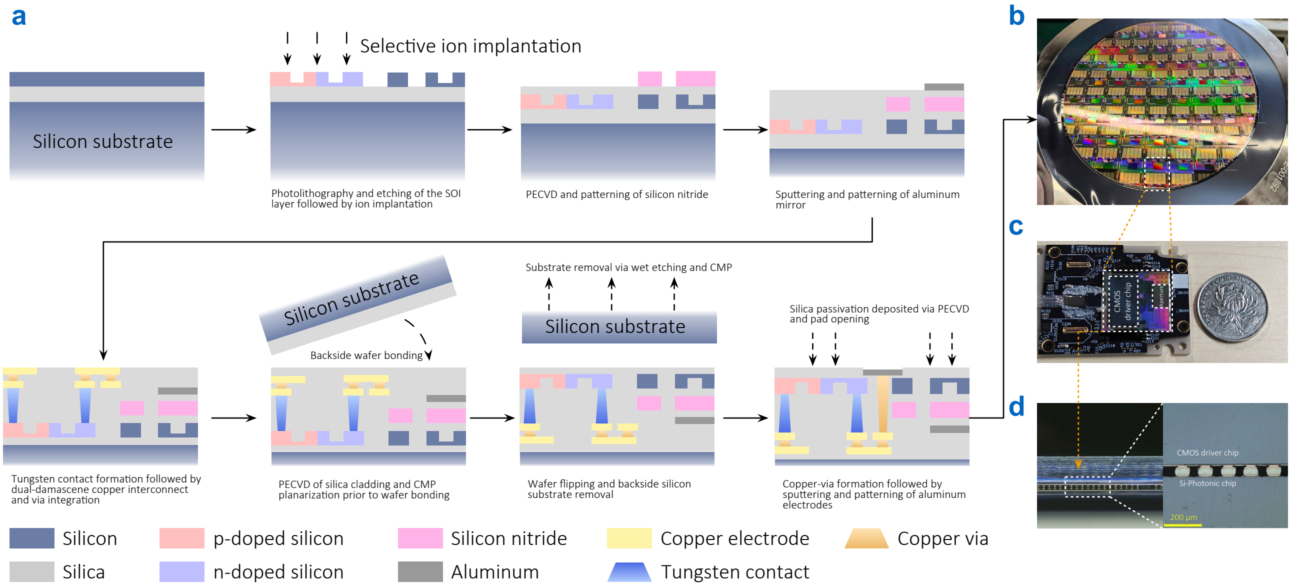

Fig. 2 | (a) Schematic of the fabrication procedure for the large-scale Si-SiN heterogeneously integrated OPA. (b) Photograph of the fabricated 8-inch silicon-photonic wafer. (c) Photograph of the fully assembled 4096-element OPA module, with a 1-Yuan coin for scale. (d) Photograph of the CMOS driver chip flip-chip bonded onto the silicon photonic integrated chip (Si-PIC), showcasing the high-density electrical integration. PECVD: plasma-enhanced chemical vapor deposition; CMP: chemical mechanical polishing.

of escalating complexity. It facilitates not only advanced heterogeneous integration with other functional photonic devices but also seamlessly supports more intricate optoelectronic integration and advanced packaging schemes required for next-generation 3D-integrated platforms.

The 8-inch silicon photonics wafer, fabricated on CUMEC's CSiP130C + BSI process platform, is shown in Fig. 2(b). Subsequently, the CMOS driver chips are co-packaged with the Si-PICs via high-density flip-chip bonding (Fig. 2(c)), providing a 10-bit control bit depth for each element. Specifically, Fig. 2(d) provides a cross-sectional view of the interconnect bumps, where a total of 9363 bumps are distributed within a 17 mm × 8.9 mm chip area. Each individual phase shifter exhibits an exceptionally low power consumption of approximately 1.5 μW/π, with a quiescent leakage current restricted to the nanoampere (nA) level. When integrated with the CMOS driver circuit, the total power consumption is approximately 1 mW per element. Consequently, the total electrical power dissipation for the entire 4096-element OPA system, including the flip-chip-bonded ASIC, is approximately 4.1 W during full-scale operation.

To meet the requirements of high-power operation, the temperature of the OPA must be maintained within a specific range, and the thermal gradient across the chip surface must be as uniform as possible. Otherwise, the thermo-optic effect of the waveguide material will introduce non-uniform parasitic phase shifts to each emission element, necessitating complex recalibration. Furthermore, high temperatures may cause material deformation, compromising the alignment and packaging precision of the fiber array at the waveguide facets, which results in fluctuations in on-chip optical power. To address these challenges, several hierarchical measures have been integrated into our design. High-density pads facilitate efficient heat exchange, transferring thermal loads from chip to chip, which are subsequently conducted to an aluminum nitride (AlN) ceramic submount. A high-performance thermoelectric cooler (TEC) system is then employed to actively dissipate heat from the submount to the external environment. Additionally, high-efficiency SiN-based edge coupler design and optimized fiber array (FA) packaging are utilized to minimize coupling loss, thereby fundamentally reducing the localized heat accumulation caused by high-power laser injection.

3 Results and discussions

3.1 Device characterization

Precise control of the emission phase is fundamental to achieving high-performance beamforming. Due to intrinsic phase errors arising from fabrication non-uniformities[47], a far-field image-based phase calibration algorithm was employed to establish a look-up table (LUT) for control voltages. For characterization, the OPA was mounted on a high-precision 2D rotation stage (BOCIC MGC102 & MRS122) with its emission aperture aligned at the center of rotation. A C-band CW laser (Santec WSL-110, 1527.7 – 1565.4 nm, 10 mW) was coupled into the device, and the far-field beam was focused via a lens (LBTEK MAD420-C) onto a short-wave infrared (SWIR) camera (Camyu

0035SW-U3) located at the focal plane.

Post-calibration results, as shown in Fig. 3(a), demonstrate a sharp beam divergence (FWHM) of 0.038° × 0.017°. The main-lobe power of the OPA was measured using a power meter (Thorlabs S145C) at a distance of 30 cm. The measured insertion loss (IL) remained within 8.7 dB–13.6 dB across the FOV, reaching 9.9 dB at the center and 11.4 dB at the edge, showing good agreement with theoretical expectations. The observed 5 dB fluctuation in insertion loss across the steering range is primarily attributed to the envelope modulation of the grating antennas. Figure 3(b) displays the overlaid 2D scanning images for the full and central FOVs. Limited by the laser tuning range of less than 40 nm, the wavelength-direction FOV was determined to be 5.2°.

Dynamic performance was evaluated by measuring the beam-switching response time between different steering angles. Two photodetectors (Thorlabs PDA10CS2) were positioned 40 cm from the chip. As shown in Fig. 3(c), the intensity transition from θ = −2° to 4° achieved a minimum response time (90% saturation) of less than 2 μs, with most angle pairs exhibiting switching speeds within 4 μs. This result defines the upper bound of the refresh rate for the current OPA LiDAR scanning system. The performance is currently limited primarily by the CMOS driver IC design; however, through further optimization of the process node and circuit architecture, the two-spot switching speed could theoretically be enhanced until the intrinsic response limit of the carrier dispersion phase shifters is reached. The functional integrity of the 4096 control units was verified through R^2 (coefficient of determination) fitting of the sinusoidal interference response (Fig. 3(d)). Approximately >

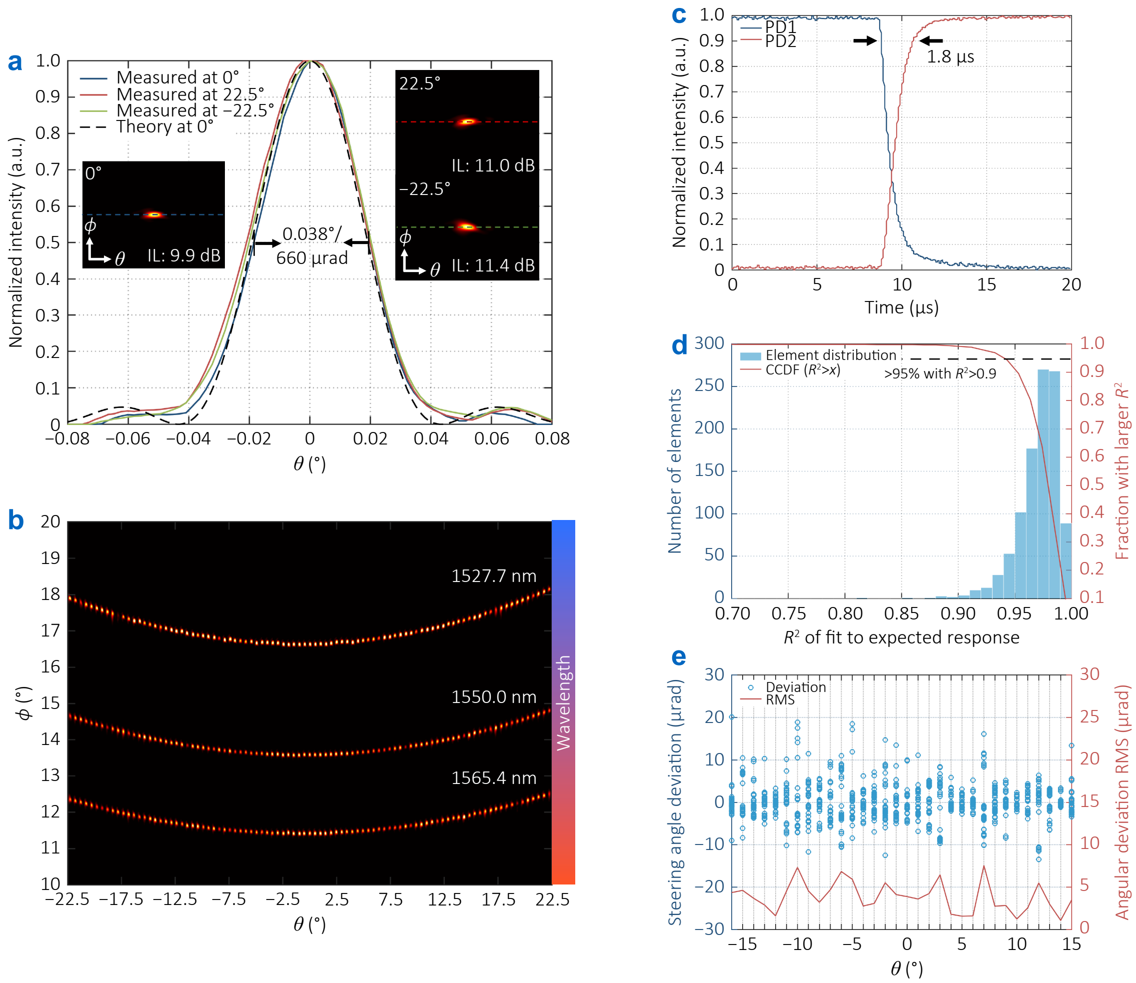

Fig. 3 | (a) Far-field beam profiles along the θ direction at center and edge field-of-view (FOV) steering angles, with measured insertion loss (IL) indicated; the dashed line represents the theoretical profile at 0° steering. (b) Two-dimensional beam steering demonstrated by superimposing far-field spots at various angles, with laser tuning from 1527.7 nm to 1565.4 nm. (c) Temporal response of two-point beam switching, measured by alternating the steering between high-speed photodetectors (PDs) for θ from −2° to 4°. (d) Effectiveness evaluation of element control via R^2 fitting of measured response curves, showing >95% functional integrity with R^2 > 0.9. (e) Beam centroid deviation during repetitive scanning (30 cycles per angle), where the red solid line indicates the root-mean-square (RMS) deviation across −16° to 15°.

95% of the units achieved an $R^2 > 0.9$, confirming high fabrication yield and ensuring superior side-lobe suppression. Furthermore, the pointing stability was characterized by tracking the beam centroid over 30 switching cycles. As shown in Fig. 3(e), the RMS pointing error within a ±15° steering range remained below 10 μrad, demonstrating the high precision and reliability of the CMOS-driven phase control system.

3.2 High-power emission demonstration

The power-handling capacity of an on-chip OPA is a critical metric that dictates the maximum detectable range in LiDAR and the achievable signal-to-noise ratio (SNR) in optical communications. To evaluate the tolerance of the device under extreme injection levels, a 1550 nm CW laser was amplified by an EDFA (Connet MFAP-1550) and injected into two channels with a combined input power of 20 W (10 W per channel). To isolate individual channel performance and prevent far-field overlapping, the beam of one channel was steered to θ = 15° while characterizing the other at the broadside.

As illustrated in Fig. 4(a), the main-lobe power at the center FOV of both channels increased linearly with injection levels, yielding a stable radiated power exceeding 700 mW per channel at 10 W/10 W input. Thermal characterization using an infrared camera (Fotric 246M-L30) showed that the fiber-chip interface reached 70 °C under full-power operation (Fig. 4(b)). Such thermal loads typically induce significant thermo-optic index perturbations, leading to parasitic phase noise and thermal-induced angular drift. However, by leveraging our enhanced thermal packaging—featuring AlN ceramic heat sinks and active TEC regulation—the insertion loss was successfully maintained within 10 dB – 12 dB with no observable degradation in beam shape, validating the robustness of the Si-SiN hybrid architecture for high-power emission.

Based on the empirical characterization, the theoretical power capacity of the OPA chip can potentially scale to 40 W (via 4×10 W injection), yielding a projected four-channel total output power exceeding 2.8 W. Currently, the primary bottleneck resides in the excessive thermal power density concentrated at the facet coupling regions. Consequently, in this demonstration, we focused on a dual-channel injection totaling 20 W. In the future, by optimizing the facet architecture and enhancing the system-level thermal packaging, the total on-chip injection power and the resulting radiation efficiency are expected to be further pushed toward their physical limits.

3.3 Coherent detection demonstration

To verify the system-level performance under practical conditions, we performed high-resolution coherent detection experiments using the 4096-element OPA LiDAR. The experimental setup (Fig. 5(a)) utilized a linearly frequency-modulated (LFM) source (INXUNTECH IXTL-03) generating a triangular frequency profile, featuring a static Lorentzian linewidth of 3 kHz, a side-mode suppression ratio (SMSR) of 55 dB, a sweep rate of 10 kHz, a tuning bandwidth of 1.08 GHz, and a frequency non-linearity below 10^{-6}. The source was divided into a local oscillator (LO) path (10%) and a transmission path (90%). The latter was amplified to 200 mW via an EDFA. A 91 m delay fiber was incorporated to introduce a frequency offset, shifting the heterodyne signal away from the low-frequency $1/f$ noise region and improving the ranging accuracy.

The backscattered signal was received through the independent R_{x1} channel and mixed with the LO. The resulting heterodyne signal was captured by a balanced photodetector (BPD, Thorlabs PDB570C) and processed by a high-speed DAQ. Benefiting from the large-aperture grating antenna design, which maximizes the effective collection area, the system achieved high sensitivity.

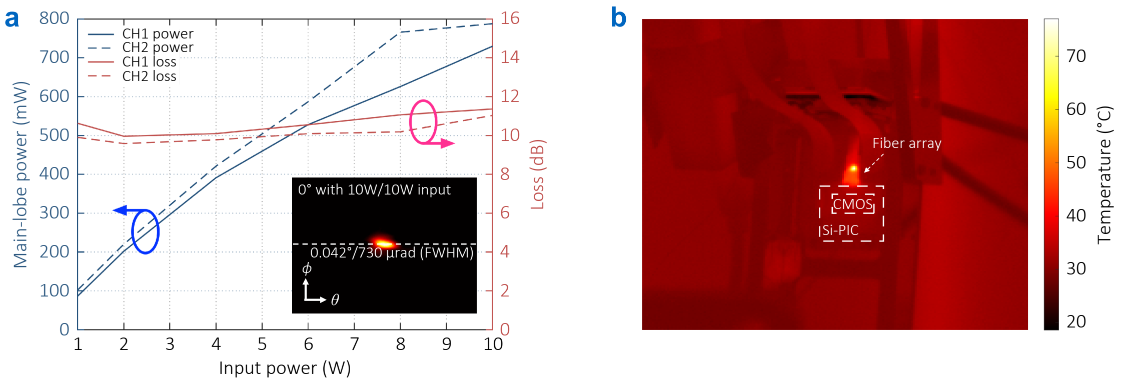

Fig. 4 | (a) Main-lobe power and insertion loss at the center FOV under 20 W injection power. Solid lines represent the main-lobe power and loss for CH1, respectively, while dashed lines represent those for CH2. All values reflect the power after reaching thermal stability. (b) Thermal camera image of the device operating under 20 W injection power.

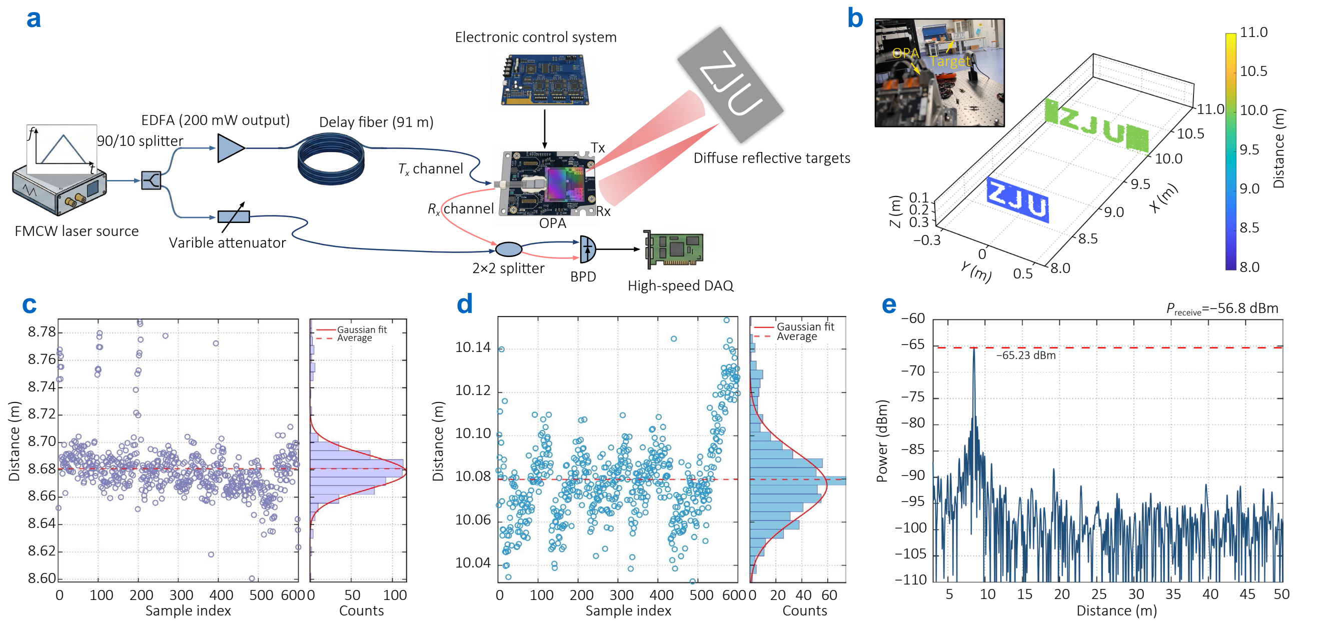

Fig. 5 | (a) Schematic of the coherent detection system. (b) Reconstructed point cloud of the detected targets. (c) Distribution and corresponding histograms of the sampling points for the foreground target (∼8.7 m) and (d) background (∼10.1 m); red dashed and solid lines represent the mean values and Gaussian fitting envelopes, respectively. (e) Measured RF power spectrum of the beat signal, with the received optical power at the R_x aperture being −56.8 dBm.

As depicted in Fig. 5(b), 3D imaging was successfully performed on a hollowed-out alphanumeric stencil target positioned at a distance of 8.7 m and a larger foam background board placed further back at 10.1 m. A longitudinal separation of 1.4 m between these two targets was clearly resolved in the reconstructed point cloud, highlighting the superior spatial resolution of the coherent LiDAR system. The detection sampling distributions for the target's foreground and background are illustrated in Fig. 5(c) and Fig. 5(d), respectively. Additionally, Fig. 5(e) displays the power spectrum of the BPD beat signal at a specific detection point on the foreground target. Furthermore, to more comprehensively evaluate the system's detection capabilities, its performance was characterized using a 90% reflectivity Lambertian calibration plate (CH-MX, Changhui Electronics Technology Co., Ltd.) at an indoor distance of 8 m under 200 mW CW injection. The measured beat-note signal-to-noise ratio (SNR) is approximately 20 dB, which is equivalent to a detection SNR of 10.5 dB for a 10% reflectivity Lambertian target. It should be noted that the current ranging capability is partially constrained by the sub-optimal collection efficiency of the Rx aperture utilized in this benchtop setup. Although this initial demonstration is restricted to an indoor range of 10 m at a modest 200 mW CW injection, synergizing these baseline results with the multi-watt power handling and large-scale coherent combining capabilities demonstrated by our OPA architecture paves the way for next-generation, ultra-long-range coherent LiDAR systems.

3.4 Synthetic aperture demonstration

Scaling integration to even larger apertures is often hindered by fabrication constraints and individual channel power thresholds. Multi-aperture coherent combining provides a scalable solution to overcome these physical limits. In this section, we demonstrate a four-channel synthetic aperture emission scheme, with 1024 elements per channel.

The experimental architecture is schematically depicted in Fig. 6(a). A coherent CW laser was split into four paths and injected into the respective OPA channels. Phase coherence between apertures was maintained using on-chip 2 × 4 mixers, which provided interference feedback to a DAQ card (NI PXIe-6738). By leveraging a 2 × 4 coherent mixer architecture, the four-step orthogonal phase detection algorithm[48] enables the instantaneous extraction of relative phase fluctuations, effectively bypassing the need for time-division computation. High-speed closed-loop phase locking was subsequently implemented via external $LiNbO_3$ modulators, achieving a control bandwidth of 6 kHz. As shown in Fig. 6(b), the phase-locked synthetic aperture successfully compressed the FWHM beam divergence to 0.017° (300 μrad), and Fig. 6(c) illustrates the rapid locking of inter-channel phase differences under closed-loop control.

The demonstrated multi-channel optical phased array (OPA) coherent combining scheme, based on silicon-on-chip mixers and PID closed-loop control, demonstrates significant technical superiority. By implementing active phase pre-compensation before the beams enter the array,

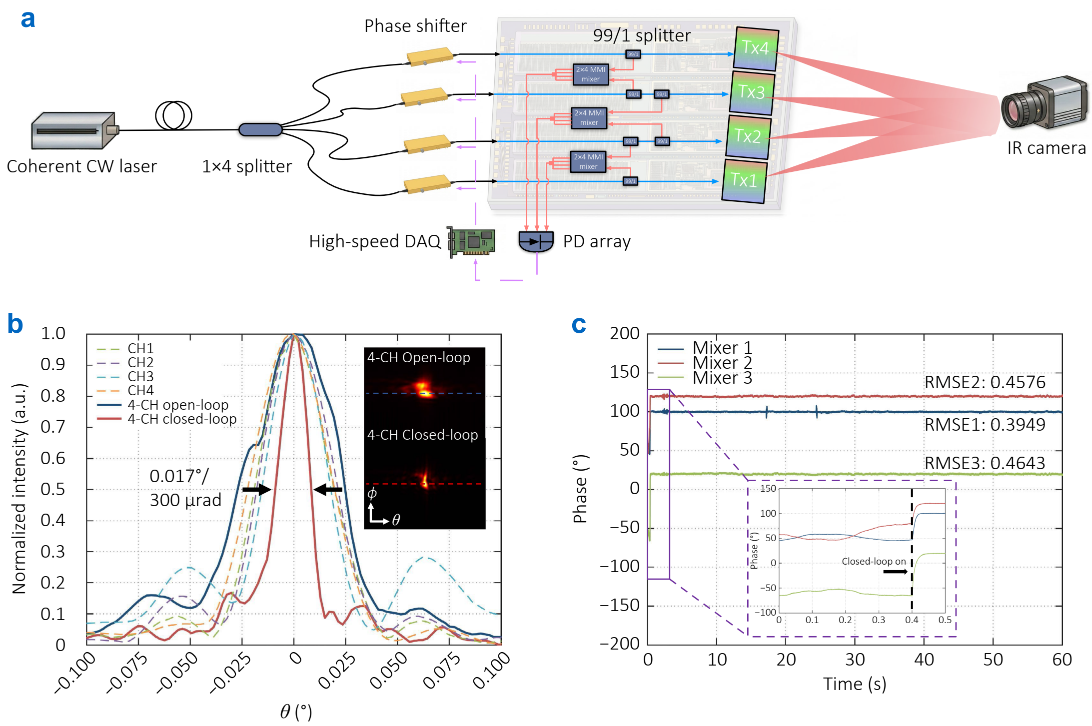

Fig. 6 | (a) Schematic of the coherent detection system. (b) Results of the closed-loop co-phasing. (c) Temporal evolutions of the reconstructed phase signals from the on-chip mixers before and after closed-loop control, with the phase RMSE of the three mixers after closed-loop control labeled.

the system not only successfully suppresses random phase errors during cross-angle scanning and achieves stable piston phase locking but also exhibits excellent compatibility with both monolithic integration and heterogeneous multi-chip architectures. Experimental data indicate that the far-field main-lobe width is compressed by over 50% following the coherent combining of the four-channel OPA. This remarkable beam convergence effectively circumvents physical limitations—such as single-waveguide power handling thresholds, nonlinear effects, and lithographic area constraints on aperture size. Furthermore, by significantly enhancing both power density and spatial resolution, it provides critical support for overcoming atmospheric attenuation, achieving high-gain LiDAR detection, and ensuring high-bandwidth, long-range optical communication links.

3.5 Discussion

To evaluate the superior performance of the heterogeneously integrated 4096-element OPA LiDAR designed in this work, we performed systematic characterizations, including device-level metrics, high-power laser emission, indoor coherent detection, and multi-channel coherent aperture synthesis. A comparison of the performance metrics of the demonstrated device with other state-of-the-art OPA LiDAR studies is summarized in Table 1. These results collectively highlight the significant potential of our architecture for long-range sensing and optical communication applications.

However, despite the immense advantages of OPAs for inertia-free steering and high-density integration, achieving kilometer-range detection with high angular resolution remains hindered by two fundamental physical constraints. First, the limited output power, which primarily stems from the laser-induced damage threshold (LIDT) of silicon or silicon nitride waveguides, nonlinear optical effects, and substantial on-chip propagation and coupling losses. Second, the restricted on-chip emission aperture, whose physical scale is strictly limited by the effective lithographic area and the scaling complexity of phase calibration for massive arrays. According to the LiDAR range equation:

$$R=\left[\frac{\eta_{\mathrm{a}}^{2}}{2\pi}\cdot LRCS\cdot\frac{A_{\mathrm{r}}}{P_{\mathrm{sens}}}\cdot\frac{P_{\mathrm{t}}\eta_{\mathrm{s}}(Nw_{x})(Mw_{y})}{\lambda^{2}}\right]^{1/4} . \quad (3)$$

In Eq. (3), R represents the maximum detection range, while η_{a} and $LRCS$ denote the one-way atmospheric transmission efficiency and the laser radar cross-section of the target, respectively. The term $A_{\mathrm{r}}/P_{\mathrm{sens}}$ characterizes the receiver performance, where A_{r} is the effective receiver aperture and P_{sens} is the sensitivity of the coherent detector. Crucially, the transmit-side performance is governed by the product of the total transmit power P_{t} and the effective emission aperture area defined by $(Nw_x)(Mw_y)$. As indicated by the fourth-root relationship, maximizing the power-aperture product (PAP) is the key to extending the operational horizon of solid-state LiDAR. Table 2 summarizes the detection ranges and the PAP for diverse practical application scenarios.

Table 1 | Summary of state-of-the-art PIC-based OPA LiDARs, listed chronologically.

Scale [ref.]	Aperture X (μm) × Y (μm)	FWHM $\Delta\theta$(°)×$\Delta\phi$(°)	Radiated power (mW) @IL (dB)	P_π per unit (mW/π)
32[49]	144 × 200	1 × 0.6	NA	160
1024[50]	2046 × 3.55	0.03 × NA	NA @20	34.7
512[21]	2000 × 5000	0.04 × 0.04	<1	0.02
512[51]	665 × 2000	0.15 × 0.08	NA	1.7
64[46]	NA	0.02 × NA	720 (pulsed) @13.8	NA
8192[37]	8000 × 5000	0.01 × 0.04	400 @11	0.302
32[52]	NA	0.09× 0.15	10	NA
64[33]	300× NA	0.6 × 0.7	0.14 @38.6	1.5-18
256[16]	1500× 10300	0.051 × 0.016	18 @19.7	19.5
9216[53]	15667 × 6000	0.05 × 0.05	NA	0.125
256[44]	1024 × 2200	0.16 × 0.04	12.59 @14	6
4096 (this work)	**8000 × 5000**	**0.017** (0.038/ch) × **0.017**	**1500 @10-11**	**1**

Table 2 | Theoretical detection ranges and required PAP for representative OPA application scenarios (assuming λ = 1550 nm, η_a^2 = 0.5, *LRCS* = 0.1 m², and P_{sens} = 1 pW), where A_r is equal to the emission aperture.

Theoretical range (km)	PAP required (W·cm²)	Typical application scenarios
0.1	0.0015	Autonomous driving and industrial robotics
1	0.72	V2X smart infrastructure and low-altitude security
10	332	Airspace surveillance and space domain awareness

Our heterogeneously integrated Si-SiN platform directly addresses these two bottlenecks: the high-power tolerance of SiN/Si structures enables a record-breaking 1.5 W CW emission, while the 4096-element integration significantly expands the equivalent emission area. In this section, the demonstrated architecture achieves a 2-ch PAP of 0.3 W·cm² (corresponding to a 20 mm² aperture and 1.5 W output power), which can theoretically reach 0.6 W·cm² after coherent combining. Furthermore, by optimizing facet coupling and system-level thermal management, it is theoretically feasible to achieve a peak PAP of 2.4 W·cm² through four-channel coherent synthesis, corresponding to a theoretical detection range of 1.57 km. Such performance would satisfy the requirements of most terrestrial or indoor applications, such as autonomous driving and industrial robotics. The substantial power margin would facilitate the implementation of multi-terminal, high-bandwidth laser communications via OPA-based beam splitting, and enable multi-beam parallel scanning in LiDAR systems to significantly enhance data throughput and frame rates without compromising the sensing range.

By further suppressing the aforementioned on-chip propagation and coupling losses—leveraging optimized edge coupling, higher-performance Si-SiN hybrid platforms, or direct monolithic source integration—while simultaneously incorporating advanced architectures such as facet emission combined with 2D steering elements (e.g., metasurfaces or liquid crystals), the total insertion loss can potentially reach an ideal threshold below 5 dB. Furthermore, with the employment of materials featuring superior power handling capabilities (e.g., SiC[54]) and the integration of multi-channel on-chip phase-locking components for multi-aperture coherent emission, the PAP of OPA LiDAR could be pushed to significantly higher regimes. This would ultimately pave the way for highly compact, fully integrated OPAs capable of ultra-long-range sensing and communication.

4 Conclusions

In conclusion, we have successfully demonstrated a high-power, large-scale, and 3D-integrated OPA LiDAR system on the Si-SiN hybrid platform. By scaling the array to 4096 elements and implementing a backside 3D routing process, we achieved a single-channel angular resolution of 0.038° × 0.017° and a synthetic aperture resolution of 0.017° × 0.017° after four-channel coherent combining, all within a compact footprint. The CMOS driver ICs are co-packaged with the Si-PIC via high-density flip-chip bonding, demonstrating an exceptional fabrication yield, with the power consumption of individual elements controlled at the 1 mW level (1.5 μW/π per phase shifter). Leveraging PN carrier-depletion phase shifters with sub-nanosecond response speeds and flip-chip bonded CMOS ICs, we achieve beam switching on the order of 2 μs. This rapid agility is pivotal for ensuring the dynamic and high-performance operation of the integrated OPA system. Our platform effectively addresses the power limitations of silicon photonics, realizing a remarkable 1.5 W main-lobe emission under 20 W CW injection while maintaining robust beam steering performance under extreme thermal loads. Furthermore, the successful integration of coherent detection and a closed-loop phase-locked four-channel synthetic aperture highlights a viable roadmap toward long-range detection and unprecedented aperture scales. These advancements represent a significant milestone in the evolution of solid-state LiDAR, paving the way for the deployment of high-performance perception systems in autonomous navigation and optical communication, ultimately bridging the gap between laboratory-scale research and mature, large-scale commercial applications.

References

1. Royo S, Ballesta-Garcia M. An overview of Lidar imaging systems for autonomous vehicles. *Appl Sci* **9**, 4093 (2019).
2. Hu MX, Pang YJ, Gao L. Advances in silicon-based integrated Lidar. *Sensors* **23**, 5920 (2023).
3. Editorial. LiDAR drives forwards. *Nat Photonics* **12,** 441 (2018).
4. Xu WH, Yuan QQ, Yang YH et al. Progress and prospects for LiDAR-oriented optical phased arrays based on photonic integrated circuits. *npj Nanophoton* **2**, 14 (2025).
5. Guo YH, Pu MB, Li Y et al. Surpassing the diffraction limit in long-range laser engineering via cross-scale vectorial optical field manipulation: perspectives and outlooks. *Opto-Electron Adv* **8**, 250256 (2025).
6. Molebny V, McManamon PF, Steinvall O et al. Laser radar: historical prospective—from the East to the West. *Opt Eng* **56**, 031220 (2016).
7. Chen RX, Shu HW, Shen BT et al. Breaking the temporal and frequency congestion of LiDAR by parallel chaos. *Nat Photonics* **17**, 306–314 (2023).
8. Ma J, Zhuo SL, Qiu L et al. A review of ToF-based LiDAR. *J Semicond* **45**, 101201 (2024).
9. Gong SJ, Tian P, Guo YH et al. Parallel all-optical encoded CDMA-driven anti-interference LiDAR for 78 MHz point acquisition. *Opto-Electron Technol* **1**, 250005 (2025).
10. Kim I, Martins RJ, Jang J et al. Nanophotonics for light detection and ranging technology. *Nat Nanotechnol* **16**, 508–524 (2021).
11. Gong SJ, Guo YH, Li XY et al. Spectral-acoustic-coordinated astigmatic metalens for wide field-of-view and high spatiotemporal resolution 3D imaging. *Light Sci Appl* **15**, 85 (2026).
12. Yu L, Wang PF, Ma PF et al. Focal plane array chip with integrated transmit antenna and receive array for LiDAR. *J Lightwave Technol* **42**, 3642–3651 (2024).
13. Hsu CP, Li BD, Solano-Rivas B et al. A review and perspective on optical phased array for automotive LiDAR. *IEEE J Sel Top Quantum Electron* **27**, 8300416 (2021).
14. Hu J, Du SP, Guo HY. Research progress on beam scanning based on liquid crystal optical phased array. *Laser Optoelectron Progress* **56**, 110002 (2019).
15. Wang XB, Guo JL, Yang ZX et al. On-chip OPA: progress and prospects in liquid crystal, lithium niobate, and silicon material platforms. *Nanomaterials* **15**, 1374 (2025).
16. Xu WH, Guo YY, Li XH et al. Fully integrated solid-state LiDAR transmitter on a multi-layer silicon-nitride-on-silicon photonic platform. *J Lightwave Technol* **41**, 832–840 (2023).
17. Sun J, Timurdogan E, Yaacobi A et al. Large-scale nanophotonic phased array. *Nature* **493**, 195–199 (2013).
18. Wang JY, Song RG, Li XY et al. Beam steering technology of optical phased array based on silicon photonic integrated chip. *Micromachines* **15**, 322 (2024).
19. Li YZ, Chen BS, Na QX et al. High-data-rate and wide-steering-range optical wireless communication via nonuniform-space optical phased array. *J Lightwave Technol* **41**, 4933–4940 (2023).
20. Derakhshandeh A, Pachnicke S, Hoeher PA. Underwater wireless laser-based communications using optical phased array antennas. *IEEE Photonics J* **15**, 7304309 (2023).
21. Poulton CV, Byrd MJ, Russo P et al. Long-range LiDAR and free-space data communication with high-performance optical phased arrays. *IEEE J Sel Top Quantum Electron* **25**, 7700108 (2019).
22. He JW, Dong T, Xu Y. Review of photonic integrated optical phased arrays for space optical communication. *IEEE Access* **8**, 188284–188298 (2020).
23. Li YZ, Chen BS, Du HL et al. Integrated optical wireless communication featured with optical phased array transceivers for full-duplex and NonLine-of-sight transmission. *Laser Photon Rev* e00822 (2025).
24. Du J, Wang J. Chip-scale optical vortex lattice generator on a silicon platform. *Opt Lett* **42**, 5054–5057 (2017).
25. Ren WB, Liang QQ, Feng JJ et al. Free-space beam shaping and steering based on a silicon optical phased array. *Photonics Res* **11**, 2093–2099 (2023).
26. Zhi ZH, Na QX, Xie QJ et al. On-chip generation of Bessel–Gaussian beam via concentrically distributed grating arrays for long-range sensing. *Light Sci Appl* **12**, 92 (2023).
27. Notaros J, Poulton CV, Raval M et al. Near-field-focusing integrated optical phased arrays. *J Lightwave Technol* **36**, 5912–5920 (2018).
28. Sneh T, Corsetti S, Notaros M et al. Optical tweezing of microparticles and cells using silicon-photonics-based optical phased arrays. *Nat Commun* **15**, 8493 (2024).
29. Mohanty A, Li Q, Tadayon MA et al. Reconfigurable nanophotonic silicon probes for sub-millisecond deep-brain optical stimulation. *Nat Biomed Eng* **4**, 223–231 (2020).
30. Sacher WD, Chen FD, Moradi-Chameh H et al. Optical phased array neural probes for beam-steering in brain tissue. *Opt Lett* **47**, 1073–1076 (2022).
31. Corsetti S, Notaros M, Sneh T et al. Silicon-photonics-enabled chip-based 3D printer. *Light Sci Appl* **13**, 132 (2024).
32. Raval M, Yaacobi A, Watts MR. Integrated visible light phased array system for autostereoscopic image projection. *Opt Lett* **43**, 3678–3681 (2018).
33. Yoon J, Yoon H, Kim JY et al. Demonstration of high-accuracy 3D imaging using a Si optical phased array with a tunable radiator. *Opt Express* **31**, 9935–9944 (2023).
34. Wang WXC, Lu LJ, King L et al. Cascaded subarray design and control method for power efficient, thermal crosstalk optimized optical phased array. *Opt Express* **31**, 37381–37394 (2023).
35. Poulton CV, Yaacobi A, Cole DB et al. Coherent solid-state LIDAR with silicon photonic optical phased arrays. *Opt Lett* **42**, 4091–4094 (2017).
36. Li YZ, Chen BS, Na QX et al. Wide-steering-angle high-resolution optical phased array. *Photonics Res* **9**, 2511–2518 (2021).
37. Poulton CV, Byrd MJ, Russo P et al. Coherent LiDAR with an 8, 192-element optical phased array and driving laser. *IEEE J Sel Top Quantum Electron* **28**, 100508 (2022).
38. Chen BS, Li YZ, Na QX et al. Demonstrated high-frame-rate real-time 4D imaging of optical phased array solid-state LiDAR system. In *Optical Fiber Communication Conference (OFC) 2025* M2J. 1 (Optica Publishing Group, 2025). http://doi.org/10.1364/OFC.2025.M2J.1.
39. Wang ZZ, Li XY, Ji JT et al. Fast-speed and low-power-consumption optical phased array based on lithium niobate waveguides. *Nanophotonics* **13**, 2429–2436 (2024).
40. Li WL, Zhao X, He JH et al. High-speed 2D beam steering based on a thin-film lithium niobate optical phased array with a large field of view. *Photonics Res* **11**, 1912–1918 (2023).
41. Li Y, Deng SY, Ma X et al. Narrow beam and low-sidelobe electro-optic beam steering on thin-film lithium niobate optical phased array.

Opto-Electron Sci **5**, 260002 (2026).
42. Guglielmon J, Byrd MJ, Moss BR et al. Optical phased array super-cell beyond the reticle limit. In *CLEO 2023* STh5C. 5 (Optica Publishing Group, 2023). http://doi.org/10.1364/CLEO_SI.2023.STh5C.5.
43. Liu Y, Hu H. Silicon optical phased array with a 180-degree field of view for 2D optical beam steering. *Optica* **9**, 903–907 (2022).
44. Chen BS, Li YZ, Xie QJ et al. SiN-on-SOI optical phased array LiDAR for ultra-wide field of view and 4D sensing. *Laser Photon Rev* **18**, 2301360 (2024).
45. Raptakis A, Lymperakis G, Gounaridis L et al. Sparse aperiodic optical phased arrays on polymer integration platform. *IEEE Photonics Technol Lett* **36**, 469–472 (2024).
46. Zhang LX, Li YZ, Hou Y et al. Investigation and demonstration of a high-power handling and large-range steering optical phased array chip. *Opt Express* **29**, 29755–29765 (2021).
47. Guerber S, Fowler D, Faugier-Tovar J et al. Wafer-level calibration of large-scale integrated optical phased arrays. *Opt Express* **30**, 35246–35255 (2022).
48. Yan X, Li F, Wang H et al. Coherent synthesis of silicon optical phased arrays toward enhanced power and aperture. *ACS Photonics* **13**, 373–384 (2026).
49. Hulme JC, Doylend JK, Heck MJR et al. Fully integrated hybrid silicon two dimensional beam scanner. *Opt Express* **23**, 5861–5874 (2015).
50. Chung S, Abediasl H, Hashemi H. A monolithically integrated large-scale optical phased array in silicon-on-insulator CMOS. *IEEE J Solid-State Circuits* **53**, 275–296 (2018).
51. Miller SA, Chang YC, Phare CT et al. Large-scale optical phased array using a low-power multi-pass silicon photonic platform. *Optica* **7**, 3–6 (2020).
52. Lee J, Son K, Lee C et al. Real-time LIDAR imaging by solid-state single chip beam scanner. *Electron Imag* **34**, 172 (2022).
53. Moss BR, Poulton CV, Byrd MJ et al. A 2048-channel, 125μW/ch DAC controlling a 9, 216-element optical phased array coherent solid-state LiDAR. In *2023 IEEE Symposium on VLSI Technology and Circuits (VLSI Technology and Circuits)* 1–2 (IEEE, 2023). http://doi.org/10.23919/VLSITechnologyandCir57934.2023.10185161.
54. Powell K, Li LW, Shams-Ansari A et al. Integrated silicon carbide electro-optic modulator. *Nat Commun* **13**, 1851 (2022).

Acknowledgements

This work was supported by the National Natural Science Foundation of China (Nos. 62431025, 62305344, 62405280), Leading Innovative and Entrepreneur Team Introduction Program of Zhejiang (2024R01001), and the Sichuan Provincial Natural Science Foundation-Young Scientists Fund (2026NSFSC0727).

The authors would like to express their sincere gratitude to Dr. Chen Xu for the invaluable guidance and insightful discussions throughout the experimental process.

Competing interests

The authors declare no competing financial interests.

Published by Editorial Office of *Opto-Electronic Technology*, Institute of Optics and Electronics, Chinese Academy of Sciences.